

Heterogeneous nucleation of β Sn on NiSn_4 , PdSn_4 and PtSn_4

S.A. Belyakov*, C.M. Gourlay

Department of Materials, Imperial College, London SW7 2AZ, United Kingdom

Abstract

During Pb-free soldering, β Sn often requires a high nucleation undercooling and there is an ongoing effort to develop nucleation catalysts. It is shown here that NiSn_4 , PdSn_4 and PtSn_4 are heterogeneous nucleants for β Sn, reducing the nucleation undercooling to $\sim 4\text{K}$ either when these intermetallics are present in the bulk solder or as the interfacial layer. Nucleation catalysis occurs by β Sn nucleating on the (008) facet of XSn_4 crystals with an orientation relationship (OR) $(100)\text{Sn} \parallel (008)\text{XSn}_4$ and $[001]\text{Sn} \parallel [100]\text{XSn}_4$ where there is a planar lattice match of $\sim 5\%$. This OR is also the origin of well-aligned lamellar β Sn- XSn_4 eutectic morphologies even though the eutectics contain less than 2 vol% of faceted NiSn_4 , PdSn_4 or PtSn_4 .

Key words: intermetallic compounds, heterogeneous nucleation of phase, eutectic, soldering, supercooling

1 Introduction

Tin typically exhibits a large amount of undercooling before crystallization [1]. In Sn-rich lead-free solders, common nucleation undercoolings of commercial purity (CP), bulk samples are about 25-30K [2], but maximum values can reach 90K [3]. This degree of undercooling is far beyond that typical for heterogeneous nucleation in CP engineering alloys (e.g. Al or Mg casting alloys) and this nucleation difficulty suggests that common

impurities are not effective nucleants for βSn [4]. Moreover, it has been shown that the common intermetallic compounds (IMCs) in soldering, Ag_3Sn and Cu_6Sn_5 , are ineffective at catalyzing βSn nucleation [4]. Difficult nucleation of βSn typically results in the formation of undesirable non-equilibrium solder joint microstructures with an increased volume fraction of primary IMC phases and βSn dendrites and decreased volume fraction of eutectic [4, 5]. Additionally, extensive growth of the primary IMC compounds in the undercooled liquid (e.g. Ag_3Sn blades in Sn-Ag-Cu solders) can significantly deteriorate mechanical performance of a solder joint [5, 6].

Research into the role of minor alloying elements on the nucleation undercooling of βSn have been conducted by various researchers [2, 5, 7-14] and the efficiency of many additions as catalysts of βSn nucleation in solders have been tested. However, most additions have not become successful industrial solders and the search for suitable solders with low, reproducible nucleation undercooling continues.

Our recent work on the metastable βSn - NiSn_4 eutectic [15] has shown that βSn can form interfaces with NiSn_4 with a reproducible orientation relationship (OR), a relatively good lattice match and, therefore, most likely a low interfacial energy. We note that this is one requirement of a potent heterogeneous nucleant: good atomic matching at the interface and a low interfacial energy between the nucleant and the solid to be nucleated [16, 17]. Therefore, the present study explores whether NiSn_4 and the isomorphous phases PdSn_4 , PtSn_4 and AuSn_4 can catalyse the nucleation of βSn .

Note that PdSn_4 [18], PtSn_4 [19] and AuSn_4 [18] are stable equilibrium phases with Pearson symbol *oC20* (prototype PtSn_4). Pd and Au, as well as Ni, are common metals

in the soldering industry. They are used for Electroless Nickel / Electroless Palladium / Immersion Gold (ENEPIG) and Electroless Nickel / Immersion Gold (ENIG) coatings that provide better wettability and oxidation resistance [20] and wire bonding ability [21]. Gold is also frequently used in electronics as a terminating layer in under-bump metallizations (UBM) to provide oxidation protection, and its thickness can be as large as $1\mu\text{m}$ [22]. The Au coatings dissolve into the solder during reflow and can cause formation of AuSn_4 crystals in the bulk [22]. In contrast to PdSn_4 and AuSn_4 , NiSn_4 is a metastable phase that forms during solidification (as a phase in the metastable Sn-NiSn₄ eutectic and, less commonly, as a primary phase [15, 23, 24]) and during the solid-state heat treatment of electrodeposited Sn-Ni layers [25, 26]. A number of researchers [27-31] have reported on rapid growth of a ‘plate-like’ Sn-Ni phase during ageing of Sn-Ni electroplated couples that has been termed NiSn_3 and NiSn_4 [25, 26] in different studies. Boettinger et al. [25] showed by EBSD analysis that this phase is NiSn_4 and is closely related to *oC20*- PtSn_4 . As opposed to the previous coatings, Pt is not widely used in soldering and was considered here for completeness.

We begin by measuring orientation relationships in the Sn-XSn_4 eutectics of the Sn-Ni, Sn-Pd, Sn-Pt and Sn-Au systems to test whether the Sn-NiSn₄ interfaces measured in [15] also form in other Sn-XSn_4 eutectics. We then explore the effectiveness of these *oC20-XSn₄* primary phases as catalytic substrates for βSn nucleation in bulk solders and solder joints when *oC20-XSn₄* compounds form interfacial IMC layers. Finally we explore the mechanisms of heterogeneous nucleation of βSn on *oC20-XSn₄* phases.

2 Experimental

A range of hypoeutectic, near-eutectic and hypereutectic Sn-Ni, Sn-Pd, Sn-Pt and Sn-Au alloys were prepared to study the crystallographic ORs of Sn-XSn₄ eutectics and to investigate the efficiency of XSn₄ primary crystals as catalysts of β Sn nucleation. First, master alloys of Sn-10wt%Ni, Sn-2wt%Pd, Sn-1wt%Pt and Sn-15wt%Au were produced by encapsulating the required mass of the corresponding commercial purity (CP) elements (99.9%) in an evacuated quartz ampoule, and holding at 1200°C for one week. 100g alloys were then made by mixing CP Sn with a master alloy in a graphite crucible and heating in a resistance furnace to 500°C. After 1-h holding, the melt was stirred with a preheated graphite rod, and the melt was drawn into 4 mm quartz tubes under vacuum. 4 mm solder rods were then cut into 250±10mg samples for DSC experiments in Al₂O₃ pans. A Mettler Toledo DSC was used at heating and cooling rates of 20K/min, and the peak temperatures were 350°C for near eutectic and 450°C for hyper eutectic compositions. The β Sn nucleation undercooling was defined as the difference between the onset temperature on heating and the onset on cooling.

Our previous work has shown that the formation of metastable NiSn₄ as a primary phase during the solidification of Sn-Ni alloys depends on the Ni content, the cooling rate and the impurity Fe content [15, 24]. At the relatively slow cooling rates of DSC (0.33 K/s here), primary NiSn₄ does not form in high purity Sn-Ni alloys whereas higher-Fe content alloys cause FeSn₂ crystals to form which nucleate metastable NiSn₄ [24]. Based on this, two batches of Sn-Ni alloys were made: a 'low Fe' batch using CP Sn containing ≤0.003wt% Fe (used for Sn-Ni, Sn-Pd, Sn-Pt and Sn-Au alloys) and a 'higher Fe' batch with CP Sn containing ≤0.02wt% Fe (used only for Sn-Ni alloys). Note that both Sn

batches are commercial purity grade. Both batches of Sn-Ni alloys were then tested by DSC as above to explore the role of primary metastable NiSn₄ on the nucleation of βSn.

To study the influence of an XSn₄ intermetallic layer on βSn nucleation and to compare with intermetallic layers common in soldering, commercial purity (99.9%) Ni, Pt, Pd, Au, Ag and Cu substrates were used. Each was cold rolled to 100μm, cleaned in HCl and covered with RM-5 flux (Nihon Superior Co., Ltd.). Then CP-Sn preforms (ingot rolled to 100μm and cut to 3.5x3.5mm) were placed on the fluxed substrates and these sandwiches were given an initial reflow on a hot plate at 260°C for a short time until substrate wetting occurred. The residues of the flux were removed in ethanol in an ultrasonic bath and the pre-soldered joints were placed in aluminium DSC pans (substrate side down) for further reflows while measuring nucleation undercooling.

To obtain a NiSn₄ interfacial layer, we followed previous work that reports that a metastable NiSn₄/NiSn₃ interfacial layer forms when Sn is electroplated to Ni and then heat treated at 50-140°C [27, 28, 31]. Electrodeposited Sn/Ni diffusion couples were prepared by Silchrome Plating Ltd. (Leeds, UK). 100mm x 100mm x 0.5mm Cu sheets were first electroplated with a Ni layer (2-3μm) and then with a Sn layer (10-20μm). The plating current density for Ni and Sn were 2A/dm² and 1A/dm² respectively. Tinmac Stannolyte and Nimac Stellar solutions were used for bright Sn and bright Ni electrodeposition respectively. These couples were then solid-state heat treated at 50°C for 1200h to grow relatively large NiSn₄ plates. The plated sheets were then cut into 3.5x3.5mm coupons for DSC experiments.

For all joints and plated sheets, a Mettler Toledo DSC was used to perform further reflows while measuring nucleation undercooling. 40 ± 5 mg solder joints were heated at rates of 10K/min and cooled at 20K/min, with a maximum temperature of 240°C and a **time above liquidus** of ~ 46 s. Each solder joint was cycled 5 times between 180 and 240°C. The β Sn nucleation undercooling in each experiment was measured as the difference between the onset on heating and the onset on cooling temperatures.

For subsequent microstructural investigation, all samples were mounted in Struers VersoCit acrylic cold mounting resin and wet ground to 2400 grit SiC paper followed by polishing with colloidal silica. For the investigation of the three-dimensional morphology of eutectic structures, primary intermetallic crystals and IMC layers, some samples were selectively etched with a solution of 5% NaOH and 3.5% orthonitrophenol in distilled H₂O. Specimens were immersed in the etchant at 60 °C for 3-30 min.

Specimens were then investigated using a Zeiss AURIGA Field Emission Gun scanning electron microscope (FEG-SEM) equipped with an Oxford Instruments INCA x-sight energy dispersive X-ray (EDX) detector and Oxford Instruments Nordlys S electron backscattered diffraction (EBSD) detector. Phases were identified by combining EBSD and EDX. Crystallographic orientation relationships (ORs) were studied by analysing Pole Figures generated by HKL software and by collecting and analysing pairs of diffraction **patterns** obtained from phases sharing a common interface similar to that described in [32].

3 Results

3.1. β Sn-XSn₄ eutectics

Figure 1 demonstrates representative regions of $\beta\text{Sn-XSn}_4$ eutectics formed in DSC samples after selective etching of βSn . Similar to the results in [15], the majority of eutectic formed in Sn-Ni samples in this experiment was Sn-NiSn₄ and not the equilibrium Sn-Ni₃Sn₄ eutectic. It can be seen that in all systems, the eutectic has a broken-lamellar morphology. Deep etching confirmed the 3D continuity of the lamellae which appear broken in 2D. Even though DSC provided multidirectional heat flow during solidification and, hence, multiple eutectic growth directions, the majority of eutectic regions contained lamellae aligned along distinct directions and some regions of more ‘irregular’ eutectic were also present (Figure 1B).

As can be seen from Figure 1, PdSn₄, NiSn₄ and PtSn₄ lamellae are very thin measuring less than ~50nm for PtSn₄ and less than 200nm for PdSn₄ and NiSn₄, determined by SEM-imaging after selective removal of βSn matrix. In contrast, the Sn-AuSn₄ eutectic has much thicker (up to 3.5 μm) lamellae. This is a consequence of the phase diagrams, where the Sn-PtSn₄ eutectic point is the most Sn-rich and the Sn-AuSn₄ is the least Sn-rich [33, 34], which impacts on the volume fraction of XSn₄ in the eutectic mixture and the thickness of lamellae as summarised in Table 1. The structures in Figure 1 are more regular than is common of faceted-nonfaceted eutectics [17] and formation of lamellae at such low volume fraction of XSn₄ generates a much larger $\beta\text{Sn-XSn}_4$ interfacial area than would be formed by rods [17]. Both observations indicate a strong anisotropy in the $\beta\text{Sn-XSn}_4$ interfacial energy.

Crystallographic orientation relationships (ORs) of Sn-XSn₄ eutectics are shown in Figure 2. **Figures 2A,C** provides examples of EBSD maps of the Sn-PdSn₄ and Sn-NiSn₄ eutectics

where XSn_4 lamellae are shown in dark purple. Most βSn grains have a uniform orientation (green) and the red and yellow areas adjacent to the eutectic lamellae are 62.8° βSn twins. Note that βSn twins adjacent to the XSn_4 eutectic lamellae similar to those in Figure 2A,C were observed in many samples and a similar phenomenon was observed during soldering (e.g. Figure 8F).

The distribution of βSn and XSn_4 phase orientations in Figures 2A,C are summarized as pole figures in Figure 2B,D. For clarity, the $[001]\beta Sn$ direction has been aligned with the central point in the corresponding pole figure (Figure 2B,D). As can be seen from Figure 2B, the $[100]PdSn_4$ direction matches the $[001]Sn$ direction and EBSD data analysis concluded on the following interfacial planes: $(001)PdSn_4 || (100)Sn$. The orientation relationship can be summarized as follows:

$$(001)PdSn_4 || (100)Sn \text{ and } [100]PdSn_4 || [001]Sn$$

Not all eutectic regions formed such a simple orientation relationship. To highlight this, a region of Sn-NiSn₄ eutectic that contains some regular and some ‘irregular’ eutectic is shown in Figure 2C,D. The main NiSn₄ intensity spots corresponding to the regular regions are consistent with the OR in the Sn-PdSn₄ case but the common directions are slightly misaligned between $[100]NiSn_4 || [001]Sn$. Additionally, there are weaker intensity spots corresponding to the regions of irregular eutectic. Note that the regular Sn-NiSn₄ eutectic OR derived here is consistent with results in [15]. In that case the orientation relationship was measured after controlled unidirectional solidification and a similar OR was obtained here after less controlled multidirectional solidification.

Another characteristic feature in the βSn pole figures is lower intensity spots that correspond to the 62.8° βSn twins developing along (301) plane. These twins can be seen in Figure 2A,C adjacent to the XSn_4 eutectic lamellae and are more obvious in the βSn pole figures of Sn-NiSn₄ (Figure 2D) than in Sn-PdSn₄ (Figure 2B).

For the Sn-PtSn₄ eutectic system, the OR could not be directly measured because the PtSn₄ lamellae thickness of less than $\sim 50\text{nm}$ is beyond the resolution of EBSD with the set-up used. Nonetheless, EBSD analysis of the orientation of βSn grains relative to the PtSn₄ lamellae showed that the aforementioned OR is also the case in this system since the (100) plane in βSn was parallel to the largest interface of the PtSn₄ lamellae, as in the Sn-NiSn₄ and Sn-PdSn₄ systems. Thus, the Sn-PdSn₄, Sn-NiSn₄, and Sn-PtSn₄ eutectics all develop the same OR during eutectic growth under multidirectional solidification conditions:

$$(001)\text{XSn}_4 \parallel (100)\text{Sn} \text{ and } [100]\text{XSn}_4 \parallel [001]\text{Sn}$$

The Sn-AuSn₄ eutectic appeared to be an exception to this rule. Even though AuSn₄ is isomorphous to PdSn₄ and PtSn₄ [25], EBSD analysis did not yield any reproducible ORs. Each eutectic grain appeared to have its own OR, which varied from region to region and from sample to sample. This is confirmed further in section 3.3.

3.2. Nucleation of βSn on primary XSn_4 crystals

Figure 3A demonstrates DSC results for Sn-xNi alloys containing 0-1wt%Ni with low Fe impurity level of $\leq 0.003\text{wt}\%$. The βSn nucleation undercooling decreases from $\sim 35\text{K}$ for 'pure' Sn to $\sim 12\text{K}$ for compositions above 0.2wt%Ni. Microstructural analysis showed

that primary Ni_3Sn_4 was present at $>0.2\text{wt}\%\text{Ni}$ and that Ni_3Sn_4 was the only primary Sn-Ni IMC compound formed, consistent with low Fe-containing Sn-Ni alloys studied previously [24]. This result demonstrates that dilute Ni additions significantly affect nucleation behaviour in the Sn-Ni system. However, nucleation undercoolings of $\sim 12\text{K}$ suggest that Ni_3Sn_4 is not a potent nucleant for βSn .

A distinct result was obtained whilst using Sn-Ni alloys with higher Fe levels of $\leq 0.02\text{wt}\%$. The nucleation undercooling for higher-Fe alloys decreased from $\sim 14\text{K}$ for 'pure' Sn to $\sim 3\text{-}4\text{K}$ for compositions containing $0.2\text{-}0.37\text{wt}\%\text{Ni}$ and at $\geq 0.45\text{wt}\%$ the nucleation undercooling abruptly increased back to $\sim 9\text{K}$. Microstructural analysis confirmed that a low nucleation undercooling was measured when a mixture of primary NiSn_4 and Ni_3Sn_4 crystals was present and that the abrupt increase in βSn nucleation undercooling is associated with microstructures containing only equilibrium Ni_3Sn_4 . A typical example of a microstructure containing both NiSn_4 and Ni_3Sn_4 is shown in Figure 3C. The phenomenon of NiSn_4 displacement by Ni_3Sn_4 at Ni levels $\geq 0.45\text{Ni}$ requires further investigation. The key result in Figure 3 is that a low nucleation undercooling of $\sim 3\text{-}4\text{K}$ was only measured when primary NiSn_4 was present.

Figure 4 summarizes the DSC nucleation undercooling data for Sn-rich Sn-Pt, Sn-Pd and Sn-Au alloys, and the primary phases identified by microstructural analysis of each composition are also indicated on the plots. DSC measurements in Figures 3, 4 and 7 represent results for 3-4 samples of each composition cycled 5 times (15-20 measurements). Note that no pattern was observed between the cycle number and the undercooling

As can be seen from Figure 4A-B, the β Sn nucleation undercooling is strongly affected by Pt and Pd additions and has the magnitude of $\sim 4\text{K}$ when primary PdSn_4 or PtSn_4 are present, similar to the higher-Fe Sn-Ni results when NiSn_4 is present in Figure 3B. This suggests that NiSn_4 , PtSn_4 and PdSn_4 work in a similar way catalysing β Sn nucleation. In contrast, Figure 4C shows that AuSn_4 is a relatively inefficient catalyst of β Sn nucleation.

Figure 5 shows typical primary XSn_4 crystals in the DSC samples extracted from the β Sn-matrix by selective etching. The PtSn_4 , PdSn_4 , and NiSn_4 crystals typically measured 10-50 μm in size and had a tile-like morphology typical of oC20- XSn_4 [35], whereas the AuSn_4 crystals reached millimetres in size and spanned the 4 mm DSC samples from edge to edge. In all cases, the largest facet of XSn_4 was (001) which is the XSn_4 interfacial plane in the eutectic OR shown earlier (Figure 2). Even though there were numerous XSn_4 particles available in samples of hyper-eutectic compositions (i.e. Figure 3C), metallographic investigation showed that solidified samples contained only a few β Sn grains, i.e. the presence of numerous XSn_4 particles did not result in a small β Sn grain size.

Based on DSC results showing that β Sn nucleation undercooling is significantly decreased by the presence of primary NiSn_4 , PdSn_4 , and PtSn_4 phases (Figures 3 and 4) and the fact that the XSn_4 plane involved in the preferred eutectic OR is a growth facet on primary crystals, it is likely that these XSn_4 crystals are heterogeneous nucleation sites for β Sn. Attempts were made to prove this directly by measuring the ORs between primary XSn_4 and the surrounding β Sn in DSC samples, but this was not conclusive because there were usually many primary XSn_4 crystals within one Sn- XSn_4 eutectic grain

(i.e. Figure 3C) and, therefore, it was not possible to confirm which, if any, primary XSn_4 particle was the active nucleant. However, evidence for this nucleation mechanism can be inferred from Figure 6 which shows an example of a common phenomenon for these Sn- XSn_4 systems: eutectic XSn_4 sheets growing from primary crystals ($NiSn_4$ in this case). Since the eutectic βSn grew with one OR and interfacial plane with the eutectic XSn_4 , and the eutectic XSn_4 is the same crystal as the primary XSn_4 in Figure 6, it is very likely that eutectic Sn nucleated on these primary $NiSn_4$ (001) facets with the OR in Figure 2.

In the case of hypo-eutectic compositions, the significant drop in βSn nucleation undercooling (Figures 3 and 4) can also be explained by nucleation of βSn on $NiSn_4$. In this case, eutectic $NiSn_4$ most likely nucleates first (below the eutectic temperature) and then acts as a nucleation site for βSn . Hypo-eutectic compositions have higher undercooling than hypereutectic compositions because eutectic $NiSn_4$ must nucleate as the liquid supercools with respect to the βSn liquidus in hypo-eutectic alloys whereas $NiSn_4$ already exists in hyper-eutectic compositions.

3.3 Nucleation of βSn on XSn_4 layers in solder joints

Figure 7 summarises results of the nucleation undercooling measurements when CP-Sn preforms are soldered to Ni, electroplated Sn/Ni couple (eNi), Pd, Pt, Au, Ag and Cu substrates. The measured βSn nucleation undercooling for the CP-Sn preforms without a reactive substrate was $\sim 30K$, similar to the values in Figures 3 and 4. Subsequent soldering to substrates changed this value to different extents. It can be seen that common IMC layers for soldering such as Cu_6Sn_5 and Ag_3Sn are not effective at catalysing βSn nucleation, with undercoolings of $\sim 18K$ when a Cu_6Sn_5 layer was present and $\sim 21K$

when a Ag_3Sn layer developed at the interface. Soldering to Ni produced a Ni_3Sn_4 intermetallic layer and reduced the nucleation undercooling to $\sim 8\text{K}$, similar to Figure 3A. These results are in a full agreement with the literature [36-38]. A much larger decrease in undercooling occurs when soldering to Pd and Pt substrates where a XSn_4 layer formed at the interface (Figure 8E-H), and the βSn nucleation undercooling was $\sim 3\text{K}$ similar to the results in Figure 4.

EBSD investigation of Sn/Pd and Sn/Pt solder joints which exhibited $\sim 3\text{K}$ βSn nucleation undercooling during reflow yielded the following observations: (i) the bulk solder was almost all βSn with very low fractions of eutectic, (ii) there were no primary IMC crystals in the bulk solder and (iii) the IMC layers contained columnar grains of XSn_4 with growth direction close to $[110]\text{XSn}_4$.

Figure 8 shows pole figures of the IMC layer growth textures, where it can be seen that the PdSn_4 and PtSn_4 grains grew vertically along the $[110]$ direction but are rotated to different angles around $[110]$. There were typically only one or two βSn grains above the PdSn_4 and PtSn_4 IMC layers so, similar to the solidified hypereutectic samples, it was not possible to identify which XSn_4 crystal nucleated βSn . However, the βSn grain orientation was similar in all Sn-Pd and Sn-Pt joints investigated and was related to the XSn_4 growth texture, with the $[001]\text{Sn}$ direction always close to a frequent $[100]\text{PdSn}_4$ direction among the crystals in the IMC layer (Figure 8). Furthermore, deep etching confirmed that $(001)\text{XSn}_4$ facets protrude from the top of the intermetallic layer and were, therefore, available as nucleating substrates. For instance, Figures 9B,E show typical regions of the IMC layers with examples of $(001)\text{XSn}_4$ facets protruding into what

was liquid prior to β Sn nucleation. It can be seen that the (001) planes are slightly misaligned with the normal direction to the interface. It is highly likely that the β Sn grain above the IMC layer nucleated on one of the available (001) facets of XSn_4 .

Almost identical EBSD and deep etched imaging results were obtained for Sn/Pt solder joints (Figure 8G-I). Therefore, during soldering to Pd and Pt, it is very likely that the OR observed for Sn- XSn_4 eutectics: $(001)XSn_4 \parallel (100)Sn$ and $[100]XSn_4 \parallel [001]Sn$ is the OR developed during β Sn nucleation on $PdSn_4$ and $PtSn_4$ interfacial layers.

The major observed difference, however, between the Sn/Pt and the Sn/Pd solder joints was the kinetics of the IMC layer growth during reflow. The thickness of the $SnPt_4$ IMC layer developed in the DSC experiments measured just $\sim 0.7\mu m$ compared to $55\mu m$ for $PdSn_4$ crystals grown in Sn/Pd solder joints under identical conditions. It is important to note, that Sn/Pt solder joints shown in Figure 8H-I were subjected to additional isothermal treatment at $260^\circ C$ for 10 minutes in order to grow larger $PtSn_4$ layers of $\sim 5\mu m$ before they went into the DSC. This did not change the final DSC undercooling result significantly but allowed an EBSD study of the grain orientation distribution in the IMC layer.

Soldering to a $NiSn_4$ layer in Sn/Ni electroplated couples required analysis of interfacial layer microstructures before and after soldering. The pre-existing interfacial layer in Sn/Ni electroplated couples after 1200h ageing at $50^\circ C$ contained a plate-like Ni_xSn_y phase at the Sn/Ni interface as shown in Figure 9C, similar to references [27-29, 31]. EDX measurements gave compositions in the range of Ni-(75-80at%)Sn for the plate-like phase as summarised in Table 3. The most Sn-rich measurements are $\sim 80at\%Sn$,

suggesting NiSn₄, and the most Sn-poor measurements are ~75at%Sn, suggesting NiSn₃ (Table 3). However, combined EDX and EBSD results showed that the interfacial phase in Sn-Ni electroplated couples is the same phase for all measured compositions (75-80 at%Sn) since Kikuchi patterns from the 33 plates studied could only be successfully indexed as *oC20*-NiSn₄. Note that this is the same phase as the NiSn₄ that formed during solidification in Figures 1,2,5 and 6 and [15, 23, 24]. The only difference is that the NiSn₄ formed in electroplated layers has a composition range of 75-80at%Sn (as shown in Table 3) which suggests that this phase can accommodate an excess of Ni (a depletion of Sn), whereas the NiSn₄ formed during solidification of Sn-rich alloys had more consistent composition measurements close to 80at% Sn (Table 3).

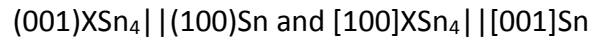
It was found that some NiSn₄ was maintained in the interfacial layer during DSC only if the maximum reflow temperature was $\leq 233^{\circ}\text{C}$ and the **time above liquidus** was ~8s. Higher temperatures or longer holding times resulted in complete decomposition of the NiSn₄ phase into liquid and Ni₃Sn₄. Remains of NiSn₄ plates after reflow in the DSC at 233°C are demonstrated in Figure 9D. The nucleation undercooling in this case was ~2-3K (labelled eNi in Figure 7), similar to soldering to Pd or Pt, and it is highly likely that NiSn₄ plates catalysed β Sn nucleation. In contrast, when the peak temperature was increased to 235°C and all the NiSn₄ phase transformed into Ni₃Sn₄ during reflow, the β Sn nucleation undercooling increased to ~ 8K, similar to values of β Sn undercooling during soldering to Ni substrates, when the only interfacial product present was Ni₃Sn₄ (Figure 7).

Note, that the presence of a XSn_4 ($X=Ni,Pd,Pt$) layer in solder joints or primary XSn_4 in bulk alloys results in significant reduction of the scatter of βSn nucleation undercooling (Figures 3, 4 and 7). Thus, XSn_4 ($X=Ni,Pd,Pt$) enhances the reproducibility of nucleation in solders.

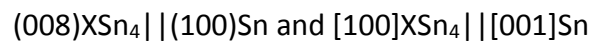
Consistent with the DSC results for the Sn-Au alloys (Figure 4C), soldering of Sn to Au substrates produced relatively high values of βSn nucleation undercooling of $\sim 15K$ (Figure 7) even though the IMC layer on the liquid side during reflow was $c20-AuSn_4$, as confirmed by EBSD. Figure 8A depicts a typical microstructure of a Sn/Au solder joint, which is comprised of very large $AuSn_4$ primary crystals growing from the $AuSn_4$ layer to the surface of the joint. Even though there were multiple growth directions of the $AuSn_4$ lamellae, EBSD showed that the joints solidified having just a few βSn grains. For instance, Figure 8C demonstrates an EBSD map of a large region of a Sn/Au solder joint capturing multiple eutectic regions that have multiple $AuSn_4$ lamellae growth directions and at the same time it contains just one major orientation for the βSn grain. Corresponding pole figures below (Figure 8D) demonstrate the distribution of the βSn and $AuSn_4$ crystal orientations for the analysed area. EBSD data analysis has not yielded any reproducible $\beta Sn/AuSn_4$ ORs in the Sn-Au system and the βSn grain orientation could not be correlated with the growth directions of the $AuSn_4$ crystals in the IMC layer (as was possible in Sn/Pd and Sn/Pt solder joints). Thus, the pole figures in Figure 8 for Sn/Au solder joints contain multiple intensity spots for $AuSn_4$ crystals and only one βSn orientation.

4. Discussion

The NiSn₄, PdSn₄ and PtSn₄ phases that catalyse the nucleation of βSn all formed the following orientation relationship with βSn:



The stated OR involves (001)XSn₄ planes as suggested by direct analysis of the pairs of EBSD patterns similar to [39]. However, comparison of the atomic densities, atomic positions and d-spacings of the planes parallel to (100)Sn and (001)XSn₄ shows that the best lattice match is between (100)Sn and (008)XSn₄ and not the (001)XSn₄ plane. Note that (100)Sn and (008)XSn₄ are the most densely packed planes in both crystals and that (008)XSn₄ planes consist of Sn atoms. In Table 4 it can be seen that the atomic density of any (008) plane in XSn₄ is 9.43-9.77 atom/nm². The comparable value for the (100) plane of Sn is 10.78 atom/nm². The stacking sequence (d-spacing) of Sn planes is about 0.29nm in βSn and about 0.28-0.29nm in XSn₄ (Table 4). Thus, the OR of the interfacial plane is as follows:



Figures 10 and 11 consider the atom matching across the interface in the deduced OR in more detail. Figure 10A shows the (100)Sn and (008)PdSn₄ planes overlapped according to the OR with the origin denoted. Please note that oC20-XSn₄ are orthorhombic crystals with 'a' and 'b' lattice parameter difference of <1%, hence, the atomic arrangement along [100] and [010] directions in XSn₄ can be treated as almost identical. The (008)XSn₄ and (100)Sn planes both involve zig-zag rows of atoms along [100] and [010] directions in XSn₄ and along the [100] direction in βSn (Figure 10), and it can be seen that every

second [100] zig-zag row provides a relatively good match and every other second [100] zig-zag row has a much larger mismatch. To quantify this, the (100)Sn plane is plotted in Figure 10B where each Sn atom is coloured based on the distance to the closest Sn atom in the (008)PdSn₄ plane. The distance is normalized to the effective spacing in [100]Sn rows in βSn, which is 2.92Å (Figure 10C).

As can be seen from Figure 10C and Table 5, the effective spacing of Sn atoms in [100]Sn and [100]XSn₄ rows have a mismatch of 9-12% for the different XSn₄ crystals relative to βSn. The d-spacing of [100] rows of Sn in βSn and XSn₄ crystals are very close with mismatch of ~0.3-0.6% for NiSn₄, PdSn₄ and PtSn₄ and slightly larger, 2.5% for AuSn₄. This low mismatch in d-spacing of Sn rows in both crystals result in a very good fit of every second Sn row at the interface (Figures 10A-B). The other half of XSn₄ rows do not provide such a good fit as they are shifted by ~0.1nm along the [100] and [010] directions in XSn₄ crystals.

Figure 11 is a 3D representation of the Sn/XSn₄ orientation relationship, which highlights the good lattice match associated with the OR. A Sn-PdSn₄ bicrystal with the deduced OR is shown opened “like a book” with the interfacial plane as the “open pages” shaded red and with [010]PdSn₄ || [001]Sn as the “spine of the book”. Atoms in the interfacial plane are shaded black and the [010]Sn and [100]PdSn₄ zig-zag rows are highlighted with bonds. The βSn and PdSn₄ unit cell orientations are shown above for clarity. Again, it can be seen that the [100]PdSn₄ and [010]Sn zig-zag rows have effective spacing mismatch of 10% and the Sn zig-zag row d-spacing is very similar in the crystals (the misfit is 0.3%). The d-spacing mismatch of (008)PdSn₄ and (100)Sn planes (the distance between the

red and the yellow planes in Figure 11) is 2.5%. This data is summarised in Table 5 for all $oC20$ - XSn_4 phases.

Table 5 shows that the lattice match is similar between βSn and each of the four XSn_4 phases and yet only three ($NiSn_4$, $PdSn_4$ and $PtSn_4$) were found to catalyse βSn nucleation. It is therefore necessary to consider why $AuSn_4$ was ineffective. We note that past work has measured the same interfacial planes in the unidirectionally grown Sn - $AuSn_4$ eutectic [40, 41], but only when a steep thermal gradient of 18-49 K/mm was applied. Those conditions were not met in the DSC of this work. One possible explanation for the inefficiency of $AuSn_4$ as a nucleant for βSn is that the effective spacing mismatch of [100] zig-zag rows is marginally worse in $AuSn_4$ than the other XSn_4 phases (Table 5) and is slightly larger than the 10% that is often considered the limit for a potent nucleant [42, 43]. A further factor that may be important and requires further work is that, while the $NiSn_4$, $PdSn_4$ and $PtSn_4$ backscattered diffraction patterns were all similar, the $AuSn_4$ EBSPs had noticeably lower band contrast under the same conditions, which might suggest a lower degree of ordering in the phase during crystal growth.

Our past unidirectional solidification study of the metastable βSn - $NiSn_4$ eutectic [15] found that two reproducible ORs could form: OR1 was $(008)NiSn_4 || (100)Sn$ with $[100]NiSn_4 || [100]Sn$ as in the present paper and OR2 was $(001)XSn_4 || (101)Sn$ with $[110]XSn_4 || [111]Sn$. The crystallography of OR2 is overviewed in [15] and provides a planar misfit of ~5%. Dufner [44] also measured OR2 in an in-situ TEM study of the growth of $PtSn_4$ into βSn in a Pt-Sn couple [44]. They showed that new (002) planes of

PtSn₄ formed at the expense of (011) planes of βSn (equivalent to (101)Sn || (001)PtSn₄). This second OR may be partly responsible for the βSn twinning in the as-solidified bulk samples or solder joints (Figures 2A,C and 8F). The {101} and {301} βSn twinning modes in Figure 12, show that during twinning, the initial (001)Sn planes (shown in red) are parallel to (10-1)Sn and (101) planes in the twinned crystals (shown in blue). Thus, if βSn twinning occurs at a βSn-XSn₄ interface with OR1, the orientation relationship becomes (001)XSn₄ || (101)Sn and [110]XSn₄ || [111]Sn which is OR2. Thus, βSn twinning at βSn-XSn₄ interfaces can maintain a good lattice match which is likely to be important in growth twinning during solidification and deformation twinning in the solid state.

Finally, it is necessary to discuss the fact that nucleation of βSn on NiSn₄, PdSn₄ and PtSn₄ did not decrease the βSn grain size. Grain refinement theories, e.g. [45], require both (i) a suitable size distribution of potent nuclei and (ii) the development of significant constitutional supercooling ahead of solid-liquid interfaces in which new nucleation events can occur. This work has shown that NiSn₄, PdSn₄ and PtSn₄ are active heterogeneous nuclei. To reduce the grain size, future work should consider combining this with solute that provides strong growth restriction.

5. **Conclusions**

This paper has shown that NiSn₄, PdSn₄ and PtSn₄ crystals are nucleation sites for βSn, reducing its nucleation undercooling from ~35K for CP-Sn to 3-4K.

A crystallographic study of multidirectionally solidified eutectics showed that βSn-NiSn₄, βSn-PdSn₄ and βSn-PtSn₄ eutectics form highly aligned structures of very thin XSn₄

lamellae ($\leq 200\text{nm}$) resulting in virtually one low energy interface with βSn . EBSD confirmed the orientation relationship (OR) of the interfacial plane to be: $(008)\text{XSn}_4 \parallel (100)\text{Sn}$ and $[100]\text{XSn}_4 \parallel [001]\text{Sn}$. This lamellar interface involves the planes and the directions with highest atomic densities in both phases and has an average lattice mismatch of only $\sim 5\%$.

Primary NiSn_4 , PdSn_4 and PtSn_4 were found to be efficient catalysts of βSn nucleation. Solidification of hypereutectic binary alloys demonstrated that NiSn_4 , PdSn_4 and PtSn_4 crystals of $10\text{-}50\mu\text{m}$ in size reduce the βSn nucleation undercooling from $\sim 35\text{K}$ to $3\text{-}4\text{K}$. Nucleation of βSn on the (001) facet of the XSn_4 crystals generates the same OR measured during eutectic growth.

A similar large decrease in βSn nucleation undercooling to values of $\sim 3\text{K}$ occurred during soldering when the IMC layer formed during interfacial reactions was PdSn_4 , PtSn_4 or NiSn_4 . This was shown to occur during soldering to Pd and Pt substrates as well as during reflow of aged Sn/Ni electroplated couples where an interfacial NiSn_4 layer already existed. In Sn-Pd and Sn-Pt joints, it was shown that XSn_4 IMC layers grow along the [110] direction and have (001) XSn_4 facets readily available for βSn nucleation.

Despite having an isomorphous *oC20* crystal structure, AuSn_4 has been found to be an ineffective catalyst of βSn nucleation, both as a primary phase in hypereutectic alloys and as an interfacial layer during soldering to Au substrates. Additionally, the βSn - AuSn_4 eutectic did not grow with a reproducible OR during multidirectional solidification. It was shown that the βSn - AuSn_4 lattice match is marginally worse than the other βSn - XSn_4 interfaces.

References

1. Kang SK, Cho MG, Lauro P, Shih DY, J Mater Res 2007;22:557.
2. Cho MG, Kim HY, Seo SK, Lee HM, Appl Phys Lett 2009;95:2.
3. Kang SK, Cho MG, Lauro P, Shih DY, 2007 Proceedings - 57th Electronic Components & Technology Conference, 2007. p. 1597-1603.
4. Swenson D, J Mater Sci-Mater in Electron 2007;18:39.
5. Kang SK, Shih DY, Leonard D, Henderson DW, Gosselin T, Cho SI et al., J Met 2004;56:34.
6. Kim KS, Huh SH, Sukanuma K, Mater Sci and Eng:A 2002;333:106.
7. Ohno A, Motegi T, J Japan Inst Met 1973;37:777
8. Buckmaster KL, Dziedzic JJ, Masters MA, Poquette BD, Tormoen GW, Swenson D, et al. 2003 TMS Fall Meeting 2003, TMS: Chicago.
9. Song JM, Huang CF, Chuang HY, J Electron Mater 2006;35:2154.
10. McCormack M, Jin S, Kammlott GW, Chen HS, Appl Phys Lett 1993;63:15.
11. Kim KS, Huh SH, Sukanuma K, J Microelectron Reliability 2003;43:259.
12. Anderson IE, Foley JC, Cook BA, Harringa J, Terpstra RL, Unal O, A, J Electron Mater 2001;30:1050.
13. Chen ZG, Shi YW, Xia ZD, Yan YF, J Electron Mater 2002;31:1122.
14. Anderson IE, Cook BA, Harringa J, Terpstra RL, J Electron Mater 2002;31:1166.
15. Belyakov SA, Gourlay CM, Intermetallics 2012;25:48.
16. Kim WT, Cantor B., Acta Metallurgica Et Materialia 1994;42:3115.
17. Dantzig JA, Rappaz M, Solidification, EPFL Press: 2009
18. Kubiak R, Wolcyrz M, JLess-Common Met 1984;97:265.
19. Schubert K, Roesler U, Zeitschrift fuer Metallkunde 1950;41:298.
20. Yoon JW, Noh BI, Jung SB, J Electron Mater 2011;40:1950.
21. Fu CH, Hung LY, Jiang DS, Chang CC, Wang YP, Hsiao CS, 2008 Proceedings - 58th Electronic Components & Technology Conference 2008, IEEE: New York. p. 1931-1935.
22. Hsiao LY, Jang GY, Wang KJ, Duh JG, J Electron Mater 2007;36:1476.
23. Belyakov SA, Gourlay CM, J Electron Mater 2012;41:3331.
24. Belyakov SA, Gourlay CM, Intermetallics 2013;37:32.
25. Boettinger WJ, Vaudin MD, Williams ME, Bendersky LA, Wagner WR., J Electron Mater 2003;32:511.
26. Chuang HY, Chen WM, Shih WL, Lai YS, Kao CR, , 2011 Proceedings - 61st Electronic Components and Technology Conference, 2011 IEEE, p. 1723-1728.
27. Haimovich J, Weld J 1989;68:S102.
28. Haimovich J, Kahn D. 1990 Proceedings - 77th AESF Annual Technical Conference, Boston: American Electroplaters and Surface Finishes Society.
29. Harman AC, Rapid Tin-Nickel Intermetallic Growth: Some Effects on Solderability, 1978, Standard Telecommunication Laboratories: Harlow.
30. Kay PJ, Mackay CA, Transactions Inst Met Finish 1977;54:68.
31. Zhang W, Clauss M, Schwager F, IEEE Transactions on Components Packaging and Manufacturing Technol 2011;8:1259.
32. Qiu D, Zhang MX, Kelly PM, Scr Mater 2009;61:312.

33. Okamoto H, J Phase Equilib Diffus, 2007;28:490.
34. Dinsdale AT., Watson A, Kroupa A, Vrestal J, Zemanova A, Vizdal J, Atlas of Phase Diagrams for Lead-Free Soldering, COST531: 2008.
35. Kubiak R, Wolcyrz M, JLess-Common Met 1985;109:339.
36. Huang YC, Chen SW, Wu KS, J Electron Mater 2010;39:109.
37. Cho MG, Kang SK, Seo SK, Shih DY, Lee HM, J Mater Res, 2009;24:534.
38. Cho MG, Kang SK, Lee HM, J Mater Res 2008;23:1147.
39. Qiu D, Zhang MA, Taylor JA, Kelly PM, Acta Mater 2009;57:3052.
40. Labullie B, Petipas C, Scr Metallurgica, 1978;12:587.
41. Favier JJ, Turpin M, Acta Metallurgica 1979;27:61021.
42. Kelly PM, Zhang MX, Metallurgical and Mater Trans A 2006;37A:833.
43. Bramfitt BL, Metallurgical Trans 1970;7:1987.
44. Dufner DC, Ultramicroscopy 1993;52:276.
45. StJohn DH, Qian M, Easton MA, Cao P, Acta Mater 2011;59:4907.

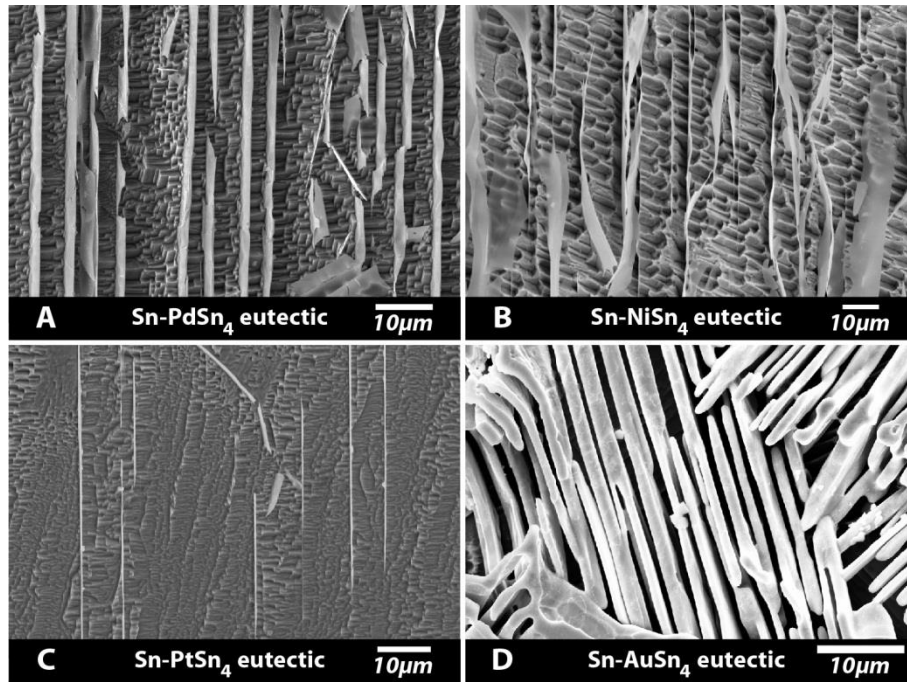


Figure 1. Representative morphologies of multidirectionally solidified Sn-XSn₄ eutectics: (A) Sn-PdSn₄, (B) Sn-NiSn₄, (C) Sn-PtSn₄, and (D) Sn-AuSn₄ eutectic. Please note the slight change in magnification

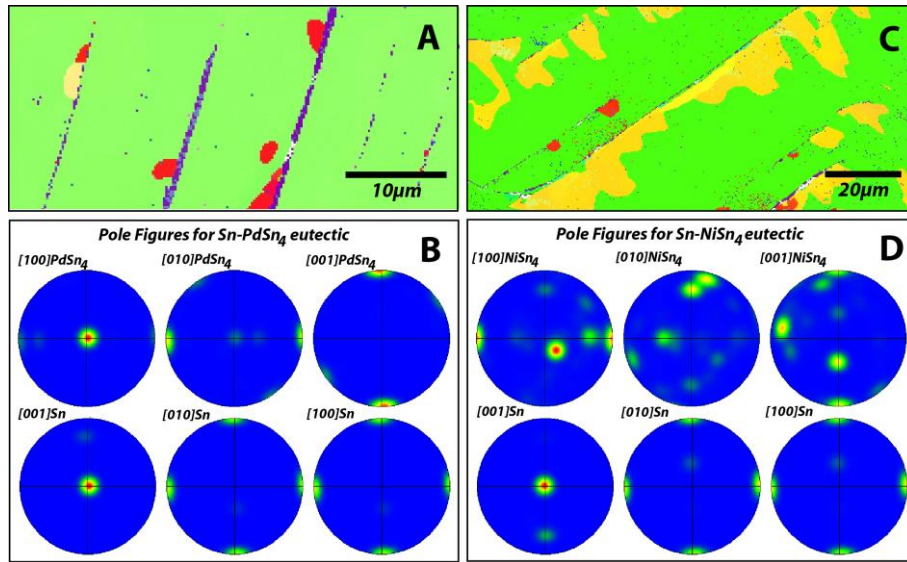


Figure 2. EBSD maps (A),(C) and corresponding pole figures (B), (D) for Sn-PdSn₄, (A-B) and Sn-NiSn₄ (C-D) eutectic regions. Please note that [010] = [100] for βSn

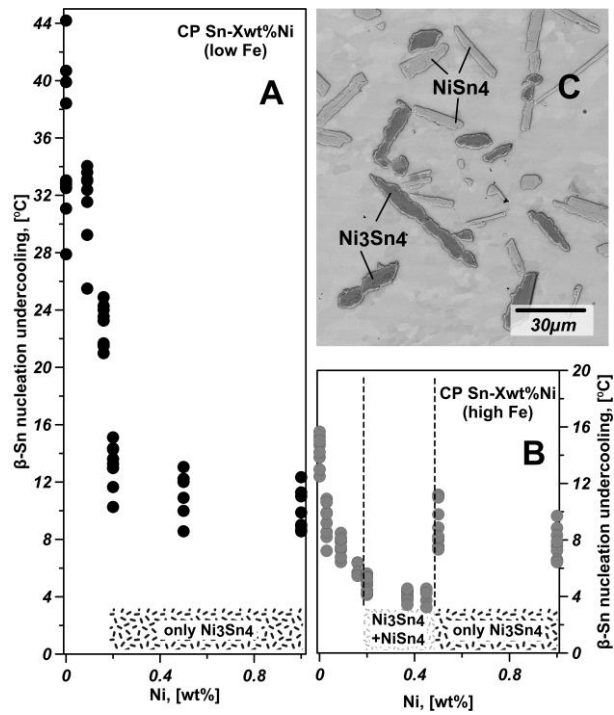


Figure 3. DSC measurements of β Sn nucleation undercooling: (A): low-Fe Sn-Ni alloys, (B) High-Fe Sn-Ni alloys and (C) BSE-SEM image of high-Fe Sn-0.37Ni containing two types of primary crystals: Ni₃Sn₄ and NiSn₄.

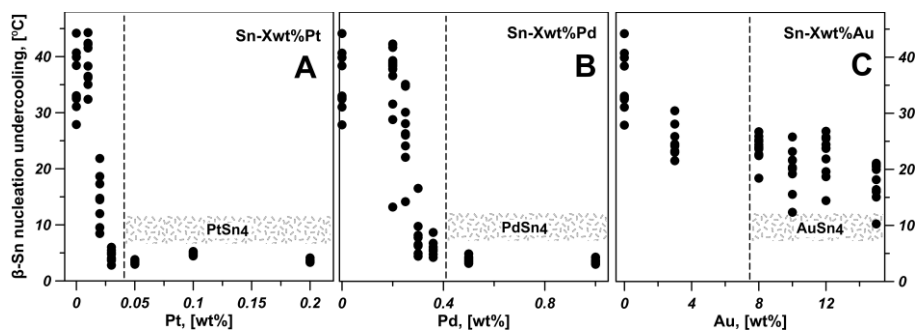


Figure 4. DSC measurements of β Sn nucleation undercooling: (A) Sn-rich Sn-Pt alloys, (B) Sn-rich Sn-Pd alloys and (C) Sn-rich Sn-Au alloys

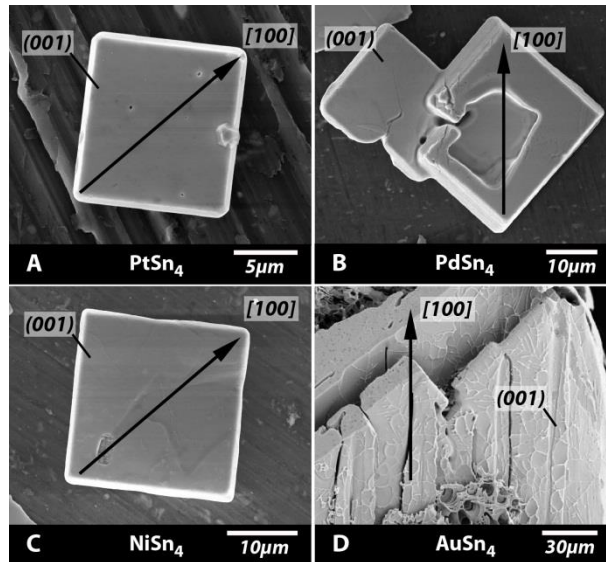


Figure 5. Representative XSn_4 primary crystals formed in: (A) Sn-0.052Pt, (B) Sn-0.5Pd, (C) Sn-0.37Ni and (D) Sn-8Au alloys

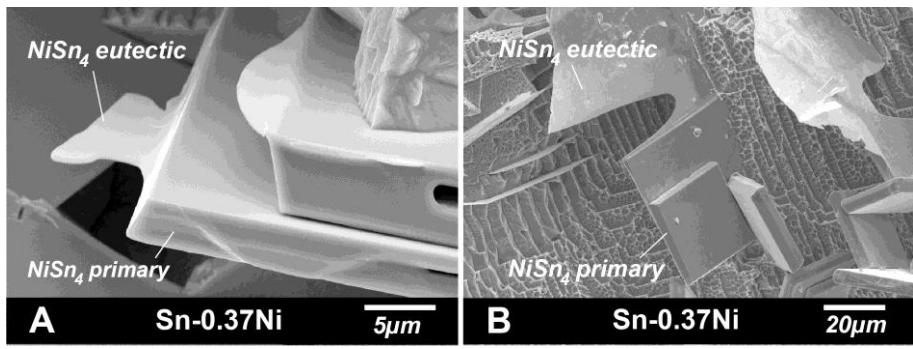


Figure 6. Examples of NiSn₄ eutectic growing off NiSn₄ primary crystals (β Sn matrix was selectively dissolved)

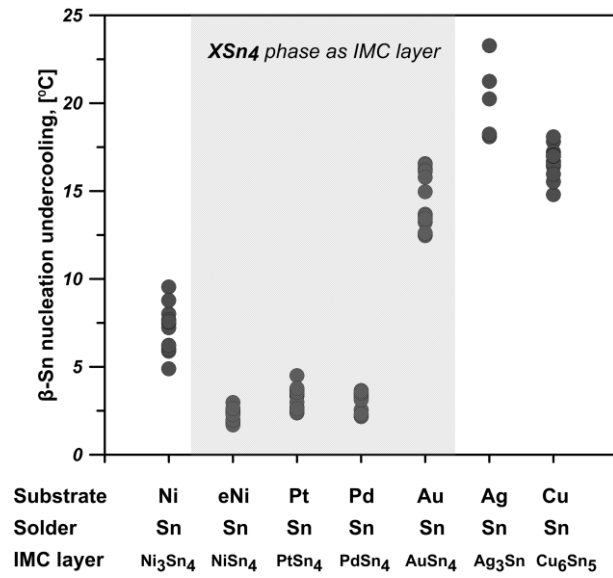


Figure 7. DSC measurements of β Sn nucleation undercooling during soldering of CP-Sn to Ni, Pt, Pd, Au, Ag and Cu substrates. IMC layers on the Sn side of solder joints are shown.

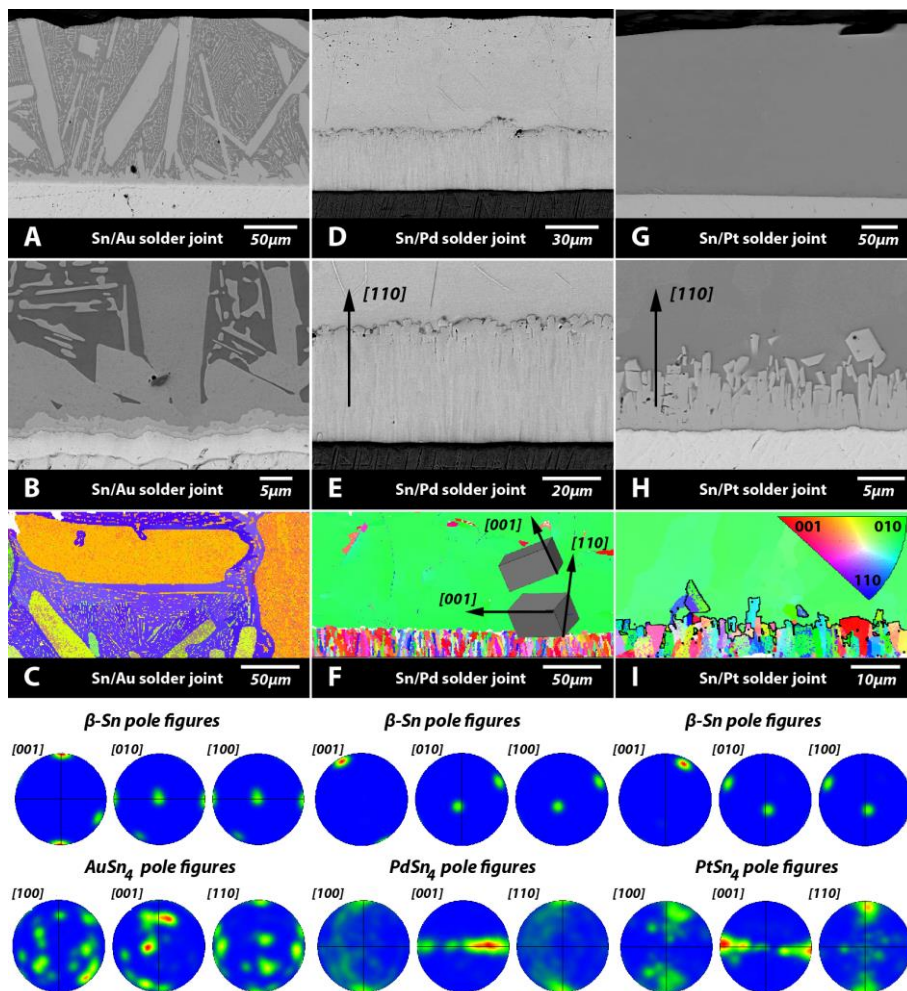


Figure 8. BSE micrographs of Sn-Au (A-B), Sn-Pd (D-E) and Sn-Pt (G-H) solder joints and corresponding EBSD maps and pole figures. Please note that $[010] = [100]$ for βSn

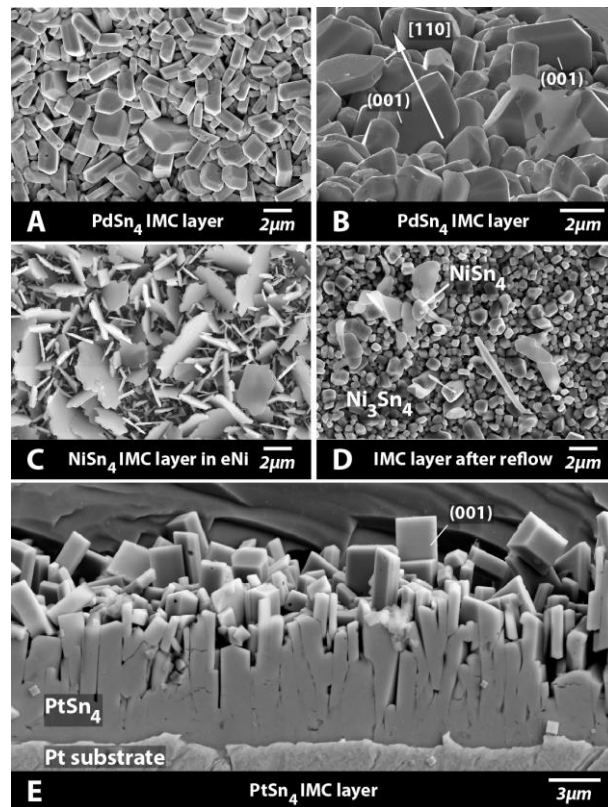


Figure 9. Typical examples of PdSn_4 IMC layers (A) view from above and (B) side view; (C) NiSn_4 interfacial IMC layer developed in Sn/Ni electroplated couples after 1200h ageing at 50C, (D) remainder of the NiSn_4 phase after reflow at 233°C and (E) typical PtSn_4 IMC layer with examples of (001) PtSn_4 facets protruding into what was liquid prior to βSn nucleation

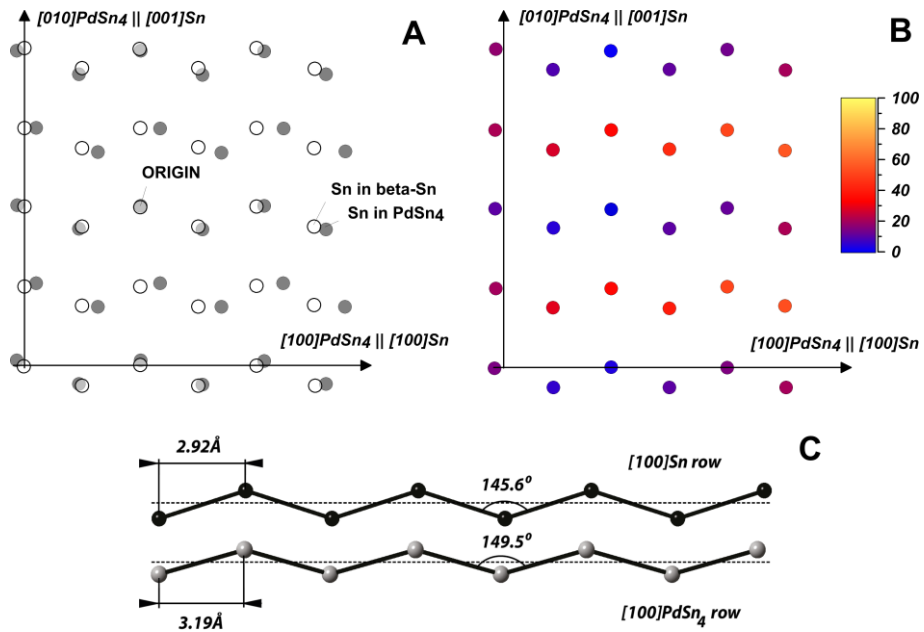


Figure 10. Atomic arrangement in the interfacial planes; (A) overlapped (100)Sn and (008)PdSn₄ planes, (B) colour map where Sn atoms in (100)Sn are coloured based on the distance to the closest Sn atom in (008)PdSn₄ normalized to the effective spacing in [100]Sn; (C) [100]Sn atom chain rows in βSn and PdSn₄ crystals.

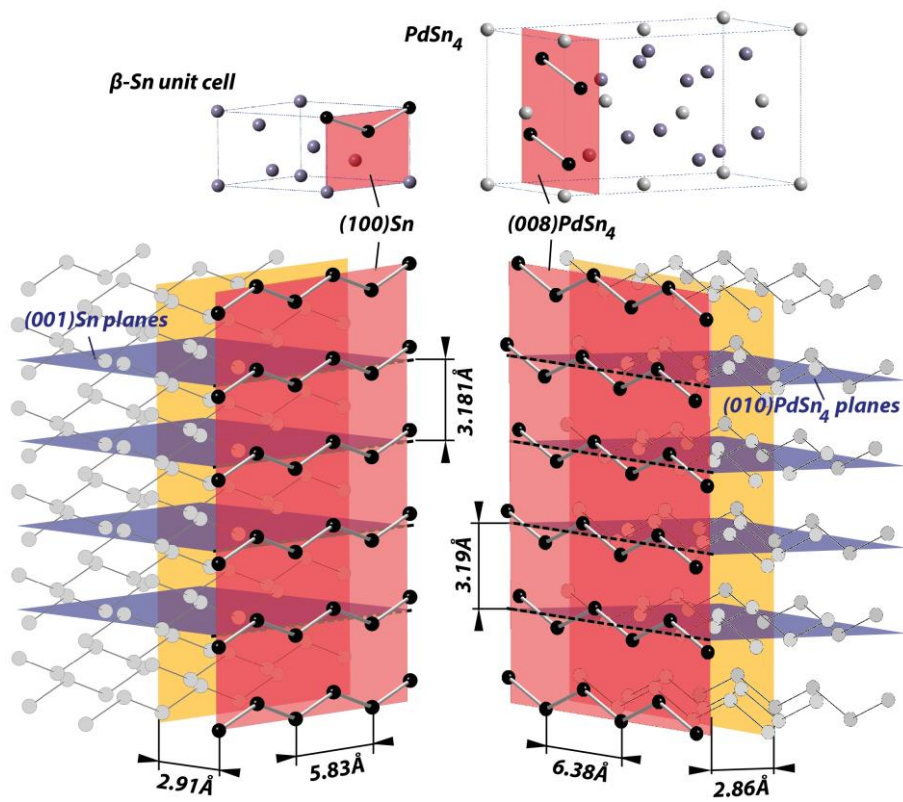


Figure 11. 3D representation of the $(008)\text{PdSn}_4 \parallel (100)\text{Sn}$ and $[100]\text{PdSn}_4 \parallel [010]\text{Sn}$ orientation relationship. Pd atoms in oC20-PdSn_4 are omitted for clarity

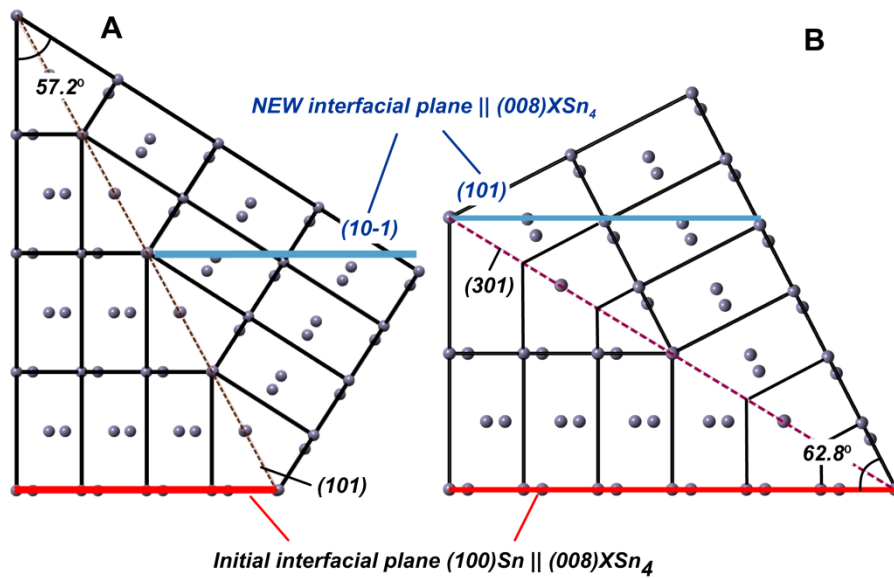


Figure 12. Projection view of the β Sn lattice on (010) plane showing the {101} and {301} β Sn twin segments. The initial interfacial plane (100)Sn is shown in red and the new interfacial plane (101)Sn developed during twinning is shown in blue.

Table 1: Predicted Sn-XSn₄ eutectic structures. ^a from [34]. ^bestimated from microstructures. ^c room temperature densities calculated from lattice parameters in [18,19,25]. ^d lamellae thickness assuming a unidirectional lamellar morphology and a spacing of 1-8 μ m.

X	C _{Sn} ^a [wt% X]	C _{Eut} ^a [wt% X]	C _{XSn₄} [wt% X]	f _{XSn₄} [wt%]	ρ_{XSn_4} ^c [g cm ³]	g _{XSn₄} [vol%]	thickness ^d [nm]
Au	0	7.41	29.32	25.3	8.98	21.5	220-1700
Pt	0	^b 0.03	29.12	0.1	9.55	0.1	1-8
Pd	0	0.36	18.31	2.0	8.19	1.7	17-136
Ni	0	0.1	11	0.9	7.68	0.9	9-72

Table 2. Compositions of the CP-Sn used for alloying in wt%, as determined by ICP-AES.
Detected levels of Cd, Al, Zn, Bi and Ag were <0.001 wt% .

Sample name	Ni	Fe	Sb	Cu	As	Pb
Higher-Fe Sn	0.001	0.02	0.006	0.002	0.001	0.046
Low-Fe Sn	0.003	0.003	0.019	0.004	0.001	0.011

Table 3. SEM-EDX results on the IMC layer observed in electroplated couples (stored for at 50°C for 1200 hours) and NiSn₄ formed during solidification of Sn-Ni alloys

Number of particles studied		Sn, at%	Ni, at%
IMC layer observed in electroplated couples			
33	Min Sn levels	75.1	24.9
	Max Sn levels	79.9	20.1
	Mean	77.2	22.8
	St. dev.	1.17	1.17
NiSn ₄ formed during solidification of Sn-Ni alloys			
40	Min Sn levels	79.6	20.4
	Max Sn levels	81.8	18.2
	Mean	81.1	18.81
	St. dev.	0.56	0.56

Table 4. Comparison of the atomic densities and d-spacings of (100)Sn, (001)XSn₄ and (008)XSn₄ planes

Phase and plane	(100)β-Sn	NiSn ₄ [25]		PdSn ₄ [18]		PtSn ₄ [19]		AuSn ₄ [18]	
		(001)	(008)	(001)	(008)	(001)	(008)	(001)	(008)
Atomic density, atom/nm ²	10.78	4.88	9.77	4.86	9.72	4.87	9.73	4.71	9.43
d-spacing, nm	0.29	0.56	0.28	0.57	0.29	0.57	0.29	0.59	0.29
Atom type	Sn	Ni	Sn	Pd	Sn	Pt	Sn	Au	Sn

Table 5. Lattice matching of (100)Sn and (008)XSn₄ planes and [010]Sn || [100]XSn₄ directions

	(100)β-Sn	NiSn₄	PdSn₄	PtSn₄	AuSn₄
Row angle, °	149.5	145.6	145.0	145.6	140.6
effective spacing [010]Sn [100]XSn ₄ mismatch, %	-	9.6	10	10	11.7
d-spacing [010]Sn [100]XSn ₄ mismatch, %	-	0.3	0.3	0.6	2.5
d-spacing (100)Sn (008)XSn ₄ mismatch, %	-	3.0	2.5	2.6	1.1